Solvent-Induced Swelling Behaviors of Microphase-Separated Polystyrene-block-

Poly(ethylene oxide) Thin Films Investigated Using In Situ Spectroscopic Ellipsometry and

Single-Molecule Fluorescence Microscopy

Herman Coceancigh, Lianjie Xue, Shinobu Nagasaka, Daniel A. Higgins* and Takashi Ito*

Department of Chemistry, Kansas State University, Manhattan, Kansas 66506-0401, USA

* To whom correspondence should be addressed.

Emails: higgins@ksu.edu (DAH), ito@ksu.edu (TI)

Abstract

Block copolymers have attracted considerable interest in the fields of nanoscience and

nanotechnology, because these polymers afford well-defined nanostructures via self-assembly.

An in-depth understanding of solvent effects on the physicochemical properties of these

microdomains is crucial for their preparation and utilization. Herein, we employed in situ

spectroscopic ellipsometry and single-molecule fluorescence techniques to gain detailed insights

into microdomain properties in polystyrene-block-poly(ethylene oxide) (PS-b-PEO) films exposed

to ethanol- and water-saturated N2. We observed a quick increase and a subsequent gradual

decrease in the ellipsometric thickness of PS-b-PEO films upon exposure to ethanol-saturated N₂.

This observation was unexpected because ethanol-saturated N₂ induced negligible thickness

change for PS and PEO homopolymer films. The similarity in maximum thickness gain observed

1

under ethanol- and water-saturated N₂ implied the swelling of PEO microdomains. Ethanol vapor permeation through the PEO microdomains was supported by the red-shift of the ensemble and single-molecule fluorescence emission of Nile red in PS-*b*-PEO films. Single-molecule tracking data showed the initial enhancement and subsequent reduction of the diffusion of hydrophilic sulforhodamine B molecules in PS-*b*-PEO films upon exposure to ethanol-saturated N₂, consistent with the spectroscopic ellipsometry results. The higher ethanol susceptibility of the PEO microdomains was attributable to their amorphous nature, as shown by FTIR data.

Introduction

Microphase separation of block copolymers (BCPs) leads to the formation of periodic, well-defined nanoscale structures based on distinct polymer components. Such self-assembled microdomains possess mechanical and physicochemical properties that are close to those of the corresponding homopolymers, yielding monolithic materials with functions reflecting the properties of the individual microdomains. The size and morphology of the microdomains can be varied by controlling the compatibility and lengths of individual polymer blocks, permitting their functions to be tuned. Owing to these unique properties, BCPs have been explored for use in various applications, including thermoplastic elastomers and adhesives, she templates for fabrication of nanopatterns and nanomaterials, polymer electrolytes, and chemical separation of nanopatterns and nanomaterials, polymer electrolytes, and chemical separation and sensing media. And the sensing media.

The physicochemical properties of BCP microdomains are often considered to be identical to those of their homopolymer counterparts. However, it was reported that microdomains have lower glass transition and melting temperatures^{16,17} and poorer crystallinity¹⁶⁻¹⁹ as compared with

the corresponding homopolymers. Similar observations were reported for polymers in nanoconfined systems, including polymers incorporated into rigid nanopores and ultrathin polymer layers sandwiched between solids. ^{20,21} In particular, polystyrene-*block*-poly(ethylene oxide) (PS-*b*-PEO) electrolytes exhibited a unique dependence of Li⁺ conductivity on PEO molecular weight, ^{22,23} which could be associated with the preferential Li⁺ distribution to the middle of the PEO microdomains ²⁴ and low ionic permeability of the PS-PEO interfacial regions. ²⁵ These observations could be explained by enhanced interfacial interactions and geometric restriction that manipulate the dynamics and packing/entanglement of the polymer chains. ^{21-23,25-27} Indeed, enhanced chain dynamics in BCP microdomains were shown using dielectric spectroscopy ^{26,28} and neutron scattering. ²⁷ The dynamic properties of polymer chains should have a significant influence on polymer–solvent interactions and associated phenomena such as solvent permeation and swelling. ²⁹ However, to the best of our knowledge, there is no prior study that unveiled the characteristics of the solvent-induced swelling of BCP microdomains through a comparison with those of their homopolymer counterparts.

A thorough understanding of solvent-induced effects on microdomain properties is crucial to control the performance of BCP-based polyelectrolytes^{8,9} and separation membranes.¹⁰⁻¹³ In addition, solvent-based treatment methods are widely employed to improve microdomain orientation in BCP films.³⁰⁻³³ The solvent-induced swelling of BCP films has been investigated by monitoring their thickness using ellipsometry^{34,35} and interferometry,³⁶ their mass using a quartz crystal microbalance,³⁷ microdomain spacing using scattering-based methods,³⁸⁻⁴⁰ and their solvent content using infrared spectroscopy.¹⁹ Swelling-induced changes in surface morphology and solute permeability were shown using atomic force microscopy (AFM)^{41,42} and fluorescence methods,^{37,43,44} respectively. Most of these studies report swelling behaviors by solvent(s) with

high compatibility to one or more of the BCP components. In contrast, the effects of poor solvents on microdomain properties attracted limited attention in spite of their critical roles in microdomain alignment. 11,45,46

In this study, we investigated the swelling behaviors of PS-b-PEO films (20–350 nm thick) (Figure 1) under ethanol- and water-saturated N₂, which will be referred to as EtOH and water vapor, respectively, using in situ spectroscopic ellipsometry and fluorescence microscopic techniques. We studied PS-b-PEO, because its solvent-treated films/membranes³⁰ were examined as polyelectrolytes, ^{8,9} lithographic masks⁵ and separation membranes. ¹² We compared results from PS-b-PEO films with those from PS and PEO homopolymer films (Figure 1) to clarify the characteristics of the swelling behaviors of the former. Ethanol is a poor solvent to both PS⁴⁷ and PEO.⁴⁸ However, hot ethanol was recently used to prepare nanoporous separation membranes from PS-b-PEO. 49,50 These reports motivated us to investigate the influences of ethanol at room temperature (ca. 20 °C) on the properties of PS-b-PEO microdomains. Water is a poor solvent to PS but a good solvent to PEO, and plays a key role in solvent vapor annealing that is widely used to control the orientation of PEO microdomains in PS-b-PEO films.³⁹ We first employed in situ spectroscopic ellipsometry to monitor film thickness upon exposure to these solvent vapors. We unexpectedly observed an increase in the thickness of PS-b-PEO films upon exposure to EtOH vapor, in contrast to PS and PEO homopolymer films. Subsequently, we sought to gain detailed insights into the effects of EtOH/water vapor exposure on the microdomain properties using fluorescence microscopic techniques: two-color ensemble and single-molecule fluorescence imaging with solvatochromic Nile red (NR; Figure 1),51-54 and single-molecule tracking (SMT)^{43,55} and fluorescence correlation spectroscopy (FCS)⁵⁶ with hydrophilic sulforhodamine B

(SRB; **Figure 1**). These measurements provide valuable information on the unique swelling behavior of PS-*b*-PEO films over the corresponding homopolymers.

Figure 1. Molecular structures of polymers (PS-*b*-PEO, PS, PEO) and fluorescent dyes (Nile red (NR) and sulforhodamine B (SRB)) used in this study.

Methods

Chemicals and Materials. All the polymers employed (Figure 1 and Table 1) were purchased from Polymer Source and used as received. Nile red (NR, Aldrich) and sulforhodamine B (SRB, Acros) were used without further purification. Ethanol (HPLC/spectrophotometric grade, Sigma-Aldrich) and toluene (HPLC grade, Fisher Chemicals) were used to prepare dye stock solutions and polymer solutions, respectively. EtOH and water vapors were generated by bubbling dry N_2 through ethanol (Decon Laboratories) and ultrapure water having a resistivity of $\geq 18 \text{ M}\Omega$ cm (Barnstead Nanopure Systems), respectively. Glass coverslips (FisherFinest® Premium; 25 x 25 mm², 0.2 mm thick) and Si (100) wafers (p-type) were purchased from Fisher and University Wafer, respectively. Gold-coated Si wafers, which were prepared by sputtering 10 nm of Ti

followed by 200 nm of Au onto Si (100) wafers, were purchased from LGA Thin Films (Foster City, CA).

Table 1. Polymers Used in This Study

polymer	manufacturer ID	$M_{\rm n}$ (PS) (g/mol)	$M_{\rm n}$ (PEO) (g/mol)	$M_{\rm w}/M_{\rm n}$
PS- <i>b</i> -PEO (13.5k–4k)	P40815-SEO	13,500	4,000	1.03
PS-b-PEO (35k-10.5k)	P19450-SEO	35,000	10,500	1.10
PS (15k)	P9746-S	15,000	_	1.09
PEO (3.8k)	P5523-EGOCH3	_	3,800	1.08
PEO (12k)	P40617-EGOCH3OH	_	12,000	1.05

Preparation and Characterization of Polymer Films. Polymer films (20-350 nm thick) were prepared on plasma-cleaned glass coverslips for fluorescence measurements, on Si substrates ($ca. 1 \times 1 \text{ cm}^2$) for atomic force microscopy (AFM), small-angle X-ray scattering (SAXS) and spectroscopic ellipsometry measurements, and on gold-coated Si substrates ($ca. 1 \times 1 \text{ cm}^2$) for FTIR external reflection spectroscopy (FTIR-ERS) measurements. These films were formed by spin-casting their toluene solution (0.4–6 wt%) on the substrates at 2000 rpm for 30 sec. For the fluorescence measurements, thin films were prepared from polymer solutions containing NR or SRB to ultimately attain a nominal dye concentration in the films in the range of 0 ~ 300 nM.

Tapping-mode AFM measurements were carried out using a Digital Instruments Multimode AFM with Nanoscope IIIa electronics and Asylum AFM probes in air. Reflection SAXS data were measured under ambient conditions using a Rigaku Smartlab diffractometer equipped with a copper target ($\lambda = 1.54$ Å).⁵⁷ The scattered X-rays, obtained at tube voltage and current of 40 kV and 44 mA, respectively, were detected with a point detector in the angular range (2θ) of 0 ~ 1.9968° with a step angle of 0.0052°. FTIR-ERS data were collected using a Nicolet iS50 FTIR spectrophotometer equipped with a Harrick Seagull reflection accessory (Pleasantville, NY) purged with N₂ and a DTGS detector.⁵⁸ All FTIR spectra were the sum of 256 scans obtained with

4 cm⁻¹ resolution at an 84° angle of incidence with respect to the substrate. The ionic impurities of the polymers were measured using inductively coupled plasma mass spectrometry (ICP-MS) upon digesting the polymers in concentrated nitric acid at 75 °C for 3 days.

In Situ Spectroscopic Ellipsometry Measurements. The thickness and refractive index (at 632.8 nm) of the polymer films were recorded by a J.A. Woollam Alpha-SE spectroscopic ellipsometer using its CompleteEASE® software. These parameters were simultaneously recorded every 12 sec under a flow of N₂, EtOH vapor, or water vapor at a flow rate of ca. 2.5 SCFH at room temperature (ca. 20 °C) (Figure S1). Film thickness gain was calculated by subtracting initial film thickness recorded under N₂ from its maximum thickness obtained under each vapor.

Wide-Field Fluorescence Measurements. An inverted fluorescence microscope with epiillumination setup (Nikon Eclipse Ti) (Figure S2ab)⁵⁶ was employed to measure ensemble and single-molecule fluorescence images for NR^{51,53,54} and SRB^{43,55,59,60} in polymer films on glass coverslips. Relatively thick films (100 – 300 nm thick) were measured to reduce the contributions of dye molecules at the film–substrate interface to the fluorescence data.⁶¹ These films nominally contained 300 nM NR for ensemble two-color measurements, 5 nM NR for single-molecule twocolor measurements, or 1 nM SRB for SMT measurements. These films were exposed to N₂, EtOH vapor, or water vapor at room temperature during the acquisition of wide-field fluorescence images/videos. Detailed instrumental setups are given in Supporting Information. (a) Two-color imaging with NR. Fluorescence emitted by NR was split to simultaneously acquire fluorescence microscopic images in two spectral bands (580 ± 20 nm and 625 ± 20 nm) using an image splitter (Cairn Research OptoSplit II) incorporating a second dichroic mirror (Chroma 605, DCLP) and two bandpass filters (Chroma 580/40 and 610/75) (**Figure S2a**). The emission ratio, E, was calculated from fluorescence signals in the 580 and 625 nm images (I_{580} and I_{625} , respectively) using the following equation: I_{625} , respectively) using the following equation:

$$E = \frac{I_{625} - I_{580}}{I_{625} + I_{580}} \tag{1}$$

Here, E values were used to qualitatively discuss the penetration of solvent vapor into polymer films rather than to quantify local dielectric constants, 53,54,62 because E is also controlled by the rigidity/fluidity of polymer matrixes around NR molecules. 51

(b) SMT Measurements with SRB. SMT measurements and analysis were carried out according to the procedure reported previously (**Figure S2b**).⁶³ Single molecule trajectories ≥ 8 consecutive frames in length were obtained with the frame-to-frame displacement of ≤ 4 pixel². This displacement threshold was selected to reduce inappropriate linking, but unfortunately also prevented measurements of quickly moving molecules. The diffusion coefficient of each molecule (D_{SMT}) was determined from its mean square displacement (MSD) as a function of lag time (τ) using Eq (2) for a two-dimensionally diffusing molecule:⁵⁶

$$MSD(\tau) = 4D_{SMT}\tau \tag{2}$$

Mobile trajectories were classified as those with $D_{\rm SMT} \ge 0.0248~{\rm pixels^2/frame}$ (= 0.0126 $\mu {\rm m^2/s}$), outside the 99.9% confidence interval of the $D_{\rm SMT}$ distribution from immobile spots.

FCS Measurements. FCS measurements were carried out for polymer films (*ca.* 300 nm thick) containing 50 nM SRB using a Nikon TE-300 inverted epi-illumination microscope (**Figure S2c**) according to a procedure reported previously.⁶³ Detailed experimental procedures are given in Supporting Information. Each autocorrelation function was fitted to a two-dimensional Fickian diffusion model, Eq (3) using the maximum entropy method (MEM).⁶³

$$G(\tau) = \sum_{i=1}^{n} a_i \left(\frac{1}{1 + \frac{\tau}{\tau_{Di}}} \right) \tag{3}$$

In this equation, τ_{Di} (= $r^2/4D_i$) and a_i (n = 200) are the characteristic diffusion time of the ith diffusion component and its contribution to the total autocorrelation amplitude, respectively. Peak D_i values, $D_{FCS,fastest}$, $D_{FCS,medium}$, and $D_{FCS,slowest}$, were compared with D_{SMT} .

Results & Discussion

In this study, we investigated the properties of thin films of PS-b-PEO (13.5k–4k) and PS-b-PEO (35k–10.5k) upon exposure to EtOH/water vapor at room temperature. These diblock copolymers have similar PEO volume fractions (≈ 0.22) with different molecular weights, and thus were anticipated to afford microdomains with a similar morphology but different dimensions. Results from the PS-b-PEO were compared with those from PS and PEO homopolymers to reveal the unique characteristics of the nanostructured polymer domains. As characterization techniques, AFM and reflection SAXS were used to verify microdomain formation in the PS-b-PEO films, and FTIR-ERS was used to assess the crystallinity of the PEO microdomains. Spectroscopic ellipsometry was employed to monitor film thickness and refractive index upon exposure to the different vapors. Finally, a series of fluorescence measurements with NR and SRB were carried out to gain insights into vapor-induced changes in the properties of the PS and PEO microdomains.

Microdomains Formed in PS-*b*-PEO Films. Microdomain formation could be verified from the AFM images of PS-*b*-PEO films (100-240 nm thick) (Figure S3). Larger microdomains were obtained from the longer PS-*b*-PEO, as shown by the microdomain spacing: 23 ± 2 and 30 ± 3 (nm) for PS-*b*-PEO (13.5k–4k) and PS-*b*-PEO (35k–10.5k), respectively. Importantly, the microdomain size and morphology were not noticeably altered upon being dried after exposure to EtOH (Figure S3cd) or water vapor (Figure S3ef). These observations could be associated with the negligible swellability of the PS microdomains by water and ethanol at room temperature that could serve as scaffolds for the PEO microdomains.

These diblock copolymers have PEO volume fraction of ~0.22, and thus were anticipated to give microdomains of a similar, possibly cylindrical, 1,2 morphology. However, their films were prepared via a spin-coating process involving quick solvent (here, toluene) evaporation, and thus the formation of microdomains was kinetically controlled. AFM cannot be used to verify microdomain formation inside these films. Thus, reflection SAXS⁵⁷ was used to gain information on microdomains inside these films. Their SAXS data exhibited a broad peak that was not found in the background spectrum obtained from a Si substrate (**Figure S4**), implying the presence of microdomains in these films. The broad peak suggests the presence of microdomains with a relatively non-uniform spacing in the range of 20-30 nm. A slight increase in 2θ after exposure to EtOH or water vapor could correspond to a slight decrease in microdomain spacing that may be associated with PEO crystallization upon the swelling-drying process, as shown by FTIR data (see below). The observation of the broad peak⁴⁰ suggests that the microdomains of these films had fairly ill-defined morphologies reflecting non-equilibrated chain conformations as a result of quick solvent evaporation during the spin-coating process.⁶⁴

Furthermore, the crystallinity of PEO microdomains in PS-b-PEO films was assessed using FTIR-ERS through a comparison with that of PEO homopolymer films. As shown in Figure S5ab, the two PS-b-PEO gave very similar spectra that included the aromatic C-H and C=C stretching bands of PS (3026 and 1601 cm⁻¹, respectively) and the C-O/C-C stretching bands of PEO (1100– 1200 cm⁻¹).^{58,65} Importantly, the C-O/C-C stretching bands of the as-cast PS-b-PEO films were relatively broad, suggesting that PEO in the PS-b-PEO was primarily present in an amorphous phase.⁶⁶ Upon exposure to EtOH vapor or water vapor and subsequent drying, the C-O/C-C stretching band at 1120 cm⁻¹ became sharper, implying the crystallization of the PEO microdomains as a result of the removal of the polar solvent. In contrast, as-cast PEO (3.8k) and PEO (12k) films afforded very sharp bands for the C-O/C-C stretching bands at 1100-1200 cm⁻¹ (Figure S5cd), reflecting the quick crystallization of the PEO homopolymers during the spincoating process. The FTIR-ERS spectra of the PEO films were unchanged after exposure to EtOH and water vapor. The lower PEO crystallinity in the as-cast PS-b-PEO films could result from the inhibition of microphase separation by the surrounding PS microdomains, especially at the PS-PEO interfacial region. 16,17,23 It should be noted that the low PEO crystallinity cannot be attributed to ionic impurities in the polymers, considering the trace concentrations (< 42 ppm) of alkaline and alkaline earth metals verified using ICP-MS.

Solvent-Induced Swelling of Polymer Thin Films. The swelling of a polymer film by solvent(s) leads to an increase in its thickness.³⁴ Here, the thickness and refractive index, n, of a thin film under different vapor conditions were monitored using spectroscopic ellipsometry. The solvent-induced swelling is anticipated to increase film thickness, and concomitantly to decrease n owing to the smaller refractive indexes of the solvents used.

Figure 2 shows typical time course data for films of (a) PS-b-PEO (13.5k-4k), (b) PS-b-PEO (35k-10.5k), (c) PS (15k) and (d) PEO (12k) under N₂ (unshaded), EtOH vapor (shaded in orange) or water vapor (shaded in blue). In these graphs, the thickness and n of the films are depicted on the left (in black) and right axes (in red), respectively. The n values of the PS and PSb-PEO films under N₂ were close to the literature and estimated values (1.589 and 1.560, respectively).⁵⁸ but that of the PEO film was significantly larger than the literature value (1.454), possibly caused by the imperfect fitting owing to its surface roughness. Exposure to EtOH vapor or water vapor led to an increase in thickness and a concomitant decrease in n for PS-b-PEO (13.5k-4k) and PS-b-PEO (35k-10.5k) films (Figure 2ab). The changes in film thickness and n were reversible (Figure 2ab), and a 6-9% thickness gain was observed regardless of the initial thickness (Figure 3ab and Table 2). These observations indicate that the entire PS-b-PEO film was swollen by these solvent vapors. Apparently, thin films of PS-b-PEO (13.5k-4k) exhibited the larger thickness gains (Figure 3ab), but statistically, the thickness gains of PS-b-PEO (13.5k-4k) and PS-b-PEO (35k-10.5k) films were not different at the 95% confidence level (**Table 2**). Of note, the slightly positive y-intercept of the least-squares regression line (offset in **Table 2**) implied the formation of a solvent layer on the PS-b-PEO films where dye molecules could diffuse quickly, as observed using SMT and FCS (see below).

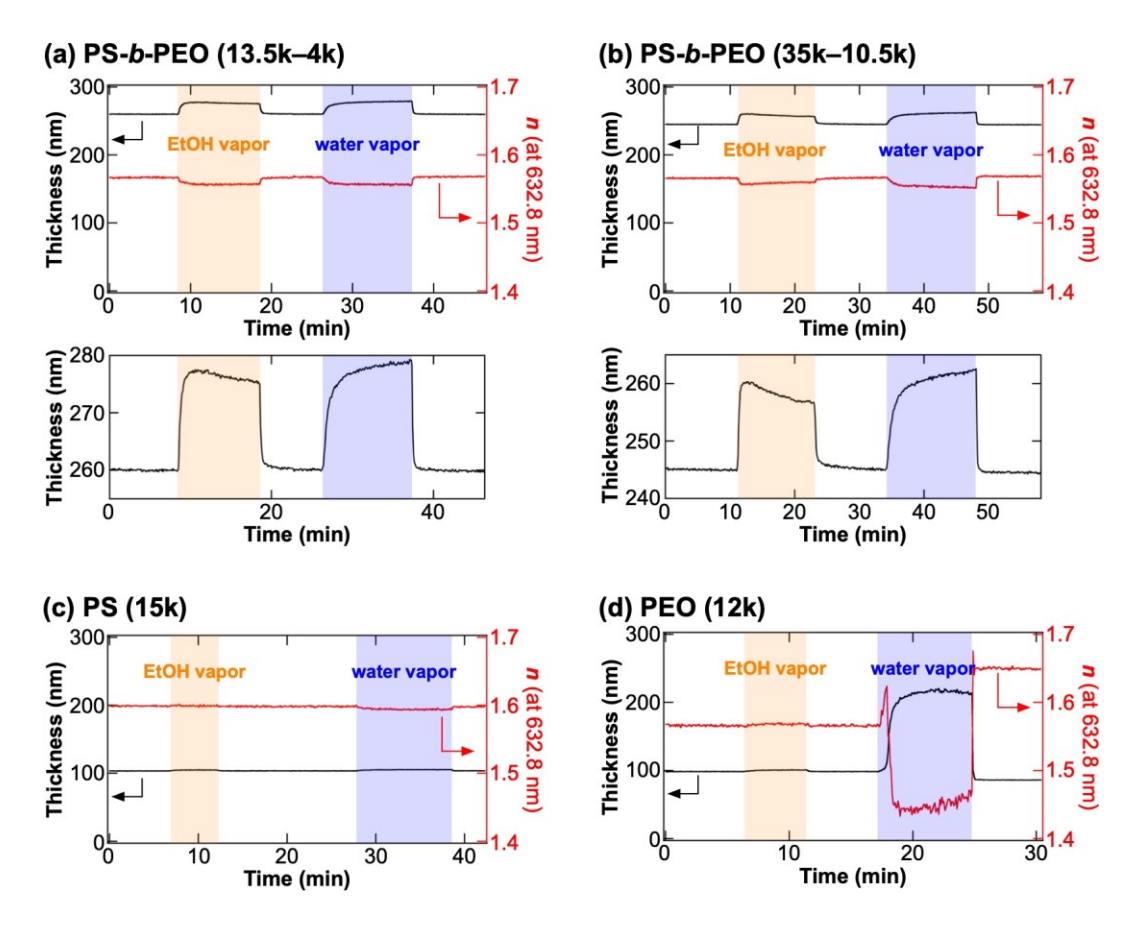


Figure 2. Typical time course data obtained with spectroscopic ellipsometry for thin films of (a) PS-b-PEO (13.5k–4k), (b) PS-b-PEO (35k–10.5k), (c) PS (15k) and (d) PEO (12k) under the flow of N₂ (unshaded), EtOH vapor (shaded in orange) and water vapor (shaded in blue) at room temperature. The ellipsometric thickness and refractive index of the films are shown in black (left ordinate) and red (right ordinate), respectively. For **Figure 2ab**, the magnified data are shown below to clarify the time-dependent thickness changes.

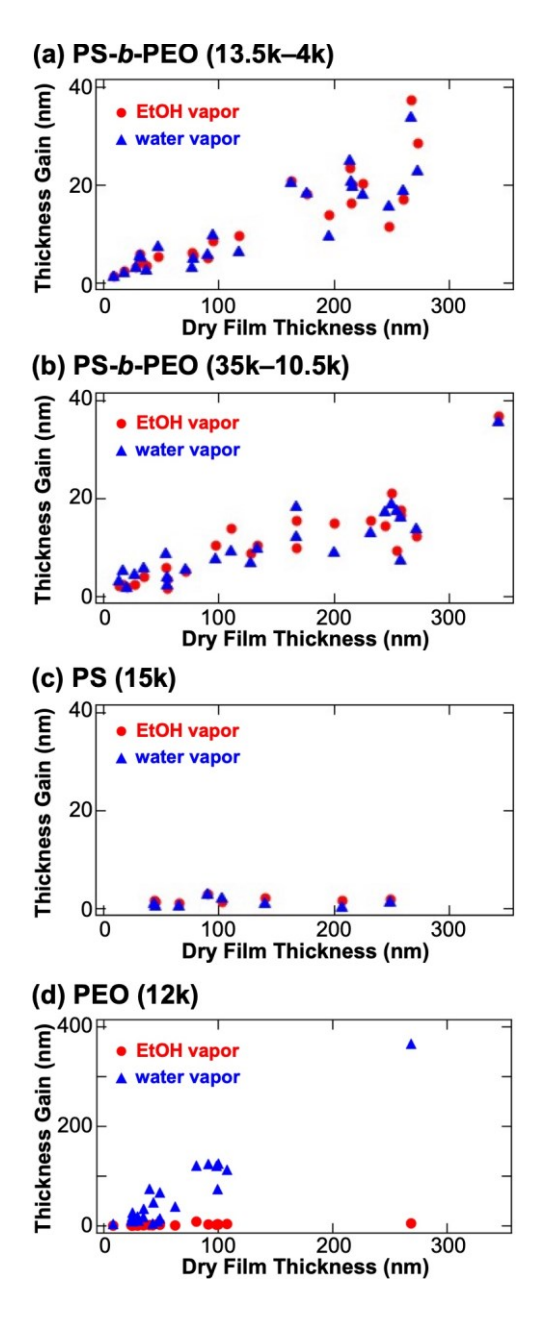


Figure 3. Plots for thickness gain as a function of initial thickness for thin films of (a) PS-*b*-PEO (13.5k–4k), (b) PS-*b*-PEO (35k–10.5k), (c) PS (15k) and (d) PEO (12k). Individual data points correspond to data obtained from individual films. Thickness gain was calculated by subtracting the thickness of an as-cast (dry) film from the maximum thickness of the same film obtained upon solvent vapor exposure.

Table 2. Solvent Vapor-Induced Thickness Gain (in %)^{a)} and Offset (in nm)^{a)} for the Polymer Films

1111101					
polymers	EtOH vapor ^{a)}		water vapor ^{a)}		
	thickness gain (%)	offset (nm)	thickness gain (%)	offset (nm)	
PS- <i>b</i> -PEO (13.5k–4k)	9.0 ± 2.2	0.3 ± 3.6	8.7 ± 2.0	0.2 ± 3.3	
PS-b-PEO (35k-10.5k)	6.9 ± 1.8	0.7 ± 3.1	6.2 ± 1.9	1.5 ± 3.3	
PS (15k)	0.2 ± 0.8	1.5 ± 1.1	-0.1 ± 1.1	1.1 ± 1.5	
PEO (12k)	2.1 ± 1.3	1.1 ± 1.0	141 ± 17	-27 ± 13	

a) 95% confidence interval obtained from the slope and y-intercept, respectively, of a least-squares regression line obtained from the data shown in **Figure 3**.

In particular, the ethanol-induced swelling of the PS-*b*-PEO films was unexpected, considering the poor compatibility of ethanol with both PS and PEO.^{47,67} Indeed, changes in the thickness and *n* of PS (15k) and PEO (12k) films were negligible or much smaller than those of the PS-b-PEO films (**Figures 2cd** and **3cd**, and **Table 2**). In addition, PEO (3.8k) films exhibited negligible thickness change under EtOH vapor (*i.e.*, 0.6–1.4 nm increase for the thickness range of 23–112 nm; data not shown). Interestingly, these PS-*b*-PEO films under EtOH vapor exhibited a thickness increase during the first few minutes and a subsequent thickness decrease (**Figure 2ab**, magnified data), which will be discussed later.

On the other hand, exposure of the PS-b-PEO films to water vapor led to a gradual thickness increase, reaching a plateau (**Figure 2ab**, magnified data). The water-induced thickness increase could be ascribed to the swelling of the PEO microdomains, as water is a good solvent for PEO. Indeed, PEO (12k) films exhibited a gradual thickness increase upon exposure to water vapor (**Figure 2d**), though changes in their ellipsometric thickness and n were not reversible owing to partial dissolution under water vapor. PEO (3.8k) films were dissolved under water vapor (data not shown). In contrast, PS (15k) films exhibited negligible thickness change under water vapor, as expected from their poor compatibility (**Figures 2c** and **3c**, and **Table 2**). Of note, the maximum thickness gain of PS-b-PEO films (PEO volume fraction $\approx 22\%$) was 6–9%, much smaller than that expected from the result of PEO films (140%) (**Figures 3abd** and **Table 2**). The significant

suppression of the thickness gain of the PS-*b*-PEO films was attributable to the unswellable PS microdomains that restricted the volume expansion of the PEO microdomains. Most importantly, the maximum thickness gain of the PS-*b*-PEO films by water vapor was very similar to that by EtOH vapor (**Table 2**), indicating that the PEO microdomains were swollen by these vapors.

These results reveal that the PS-*b*-PEO films are susceptible to EtOH-induced swelling in contrast to their homopolymer counterparts. The similarity of the maximum thickness gains under EtOH and water vapors implied the swelling of the PEO microdomains. Unfortunately, spectroscopic ellipsometry cannot provide detailed information on the swelling behaviors of the microdomains. We thus employed fluorescence microscopy methods to gain more detailed insights into the solvent-induced changes in the properties of each of the microdomains.

Polarity/Rigidity Environment in Polymer Thin Films under EtOH and Water Vapor.

The fluorescence of NR is known to be sensitive to the polarity and rigidity of its surrounding matrix, and thus was used to probe the swelling of polymer films by polar solvents. 51,69,70 Here, we assessed the fluorescence emission of NR using E values that were calculated using Eq (1) from the fluorescence intensities of an identical region or single molecule in two images simultaneously recorded in different spectral bands: 580 ± 20 and 625 ± 20 nm. 53,54 These two bands were chosen because they correspond to the emission wavelengths of NR in nonpolar and polar solvents (e.g., toluene and ethanol), respectively. 62 E is more positive under a more polar and/or less rigid environment.

First, ensemble two-color fluorescence images were measured to verify the distribution of NR in PS-*b*-PEO films. **Figure S6** shows the typical two-color fluorescence images of 200-nm thick films of the four polymers containing 300 nM NR under N₂, EtOH vapor, and water vapor.

The fluorescence of NR at 580 nm was significantly more intense than that at 625 nm in PS-b-PEO films under N₂ (**Figure S6ab**), as with that in PS films (**Figure S6c**). The PS-b-PEO films afforded E values similar to those of PS films and toluene (**Figure 4ab**). In contrast, PEO films under N₂ offered comparable fluorescence intensities at the two wavelengths (**Figure S6d**) to give a more positive E value (**Figure 4ab**), reflecting the higher polarity of PEO than PS. These results indicate that NR molecules in the PS-b-PEO films were preferentially distributed to the PS microdomains owing to their fairly low polarity. ^{53,54}

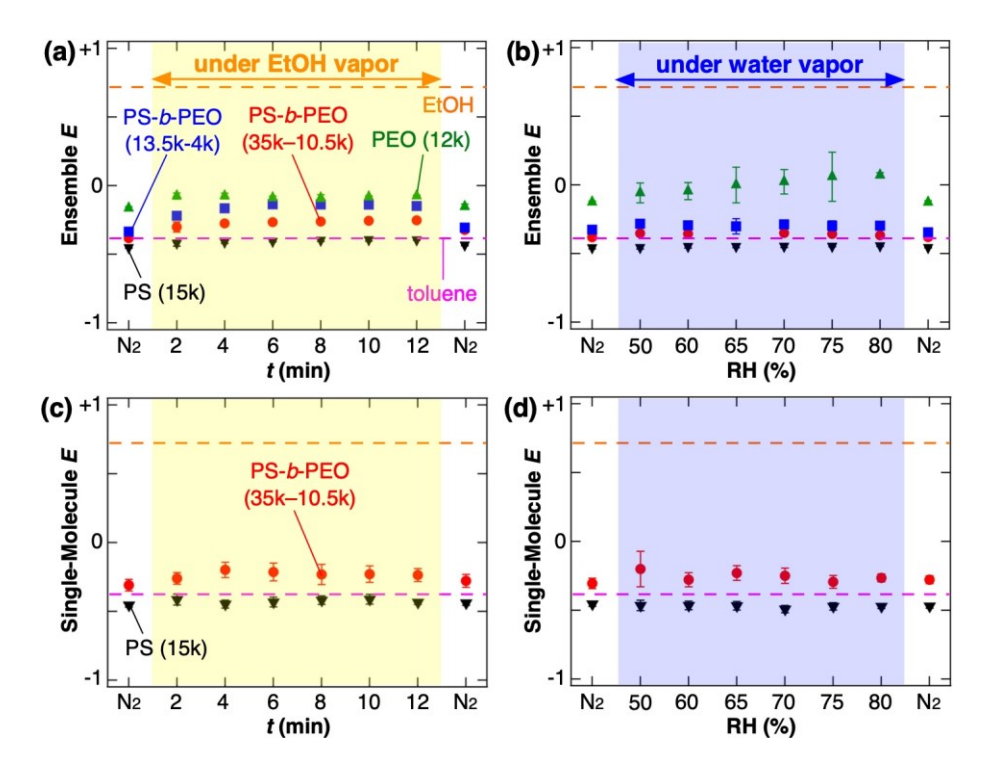


Figure 4. (a,b) Ensemble *E* values obtained from NR-containing thin films (*ca.* 300 nM, *ca.* 200 nm thick) of PS-*b*-PEO (13.5k–4k), PS-*b*-PEO (35k–10.5k), PS (15k), and PEO (12k) (a) at different EtOH vapor exposure times and (b) at different relative humidity (RH). (c,d) Single-molecule *E* values obtained from thin NR-containing films (*ca.* 5 nM, *ca.* 200 nm thick) of PS-*b*-PEO (35k–10.5k) and PS (15k) (c) at different EtOH vapor exposure times and (d) at different RH. Ensemble *E* values of 300 nM NR solutions in ethanol and toluene, which are close to previous reports, ⁶² are shown as dashed pink and orange lines, respectively. The error bars represent 95% confidence intervals obtained from *E* values of images recorded at 5-7 different areas (for a,b) and from single-molecule *E* values in images recorded at 1-10 different areas (for c,d).

Upon exposure to EtOH vapor, the NR fluorescence intensity at 625 nm slightly increased in the PS-b-PEO and PEO films to give more positive E values, while no such change was observed in the PS films (Figures 4a and S6). The change in E was observed within a few minutes upon flowing EtOH vapor, as consistent with the ellipsometric data (Figure 2). These results indicate that EtOH vapor could penetrate into PS-b-PEO and PEO films to change the environments surrounding NR molecules so they become more polar and/or less rigid. The positive E shift (Figure 4a) and negligible thickness change (Figure 3d) for the PEO films suggests they were permeable to EtOH vapor, but the packing/entanglement of the PEO chains was not strongly affected by EtOH vapor. The PS films were impermeable to EtOH vapor, as verified by negligible changes in E (Figure 4a) and ellipsometric thickness (Figure 3c). Considering the results from the homopolymer films, the positive E shift for the PS-b-PEO films under EtOH vapor was attributable to vapor permeation through the PEO microdomains, which possibly increased the local polarity of the PS-PEO microdomain boundary where some NR molecules were located. This explanation was consistent with the larger E shift observed at PS-b-PEO (13.5k-4k) than PSb-PEO (35k-10.5k) (Figure 4a), which was attributable to the higher interface/volume ratio in the films comprising the smaller microdomains.

On the other hand, PS-b-PEO films showed a much smaller change in E under water vapor, as with PS films and in contrast to PEO films, in spite of the high water-PEO compatibility (**Figure S6** and **Figures 4b**).⁶⁸ NR fluorescence at 580 nm in water vapor-exposed PS-b-PEO films was as intense as that in PS-b-PEO films under N₂ (**Figure S6ab**). These observations support the preferential distribution of NR to PS microdomains in the PS-b-PEO films.

These ensemble results were further verified by single-molecule two-color fluorescence data^{53,54} obtained from 200-nm thick films. **Figures 5** and **S7** shows fluorescence images recorded for thin films of the four polymers with and without 5 nM NR, respectively. The presence of NR offered the larger number of fluorescent spots per video for PS-*b*-PEO and PS films (**Figures 5a-c** vs. **S7a-c**), but not for PEO films (**Figures 5d** vs. **S7d**). Fluorescence from NR molecules was generally more intense than that from impurities, as shown by fluorescence intensity histograms (**Figure S8**). The negligible single-molecule fluorescence from NR in PEO (**Figure S8d**), as well as the weaker ensemble fluorescence (**Figure S6d**), could be ascribed to the reduction of the quantum efficiency of NR in polar environments. ^{51,69,70} More importantly, many single molecules in PS-*b*-PEO and PS films under N₂ offered more intense fluorescence at 580 nm (**Figure 5a-c**) to give negative *E* (**Figure S9a-c**), confirming that single NR molecules were mainly present in non-polar environments in these films. Of note, most of NR molecules in PS-*b*-PEO and PS films were immobile under EtOH and water vapor (data not shown), supporting their preferential distribution to the PS microdomains that were not swellable by ethanol and water.

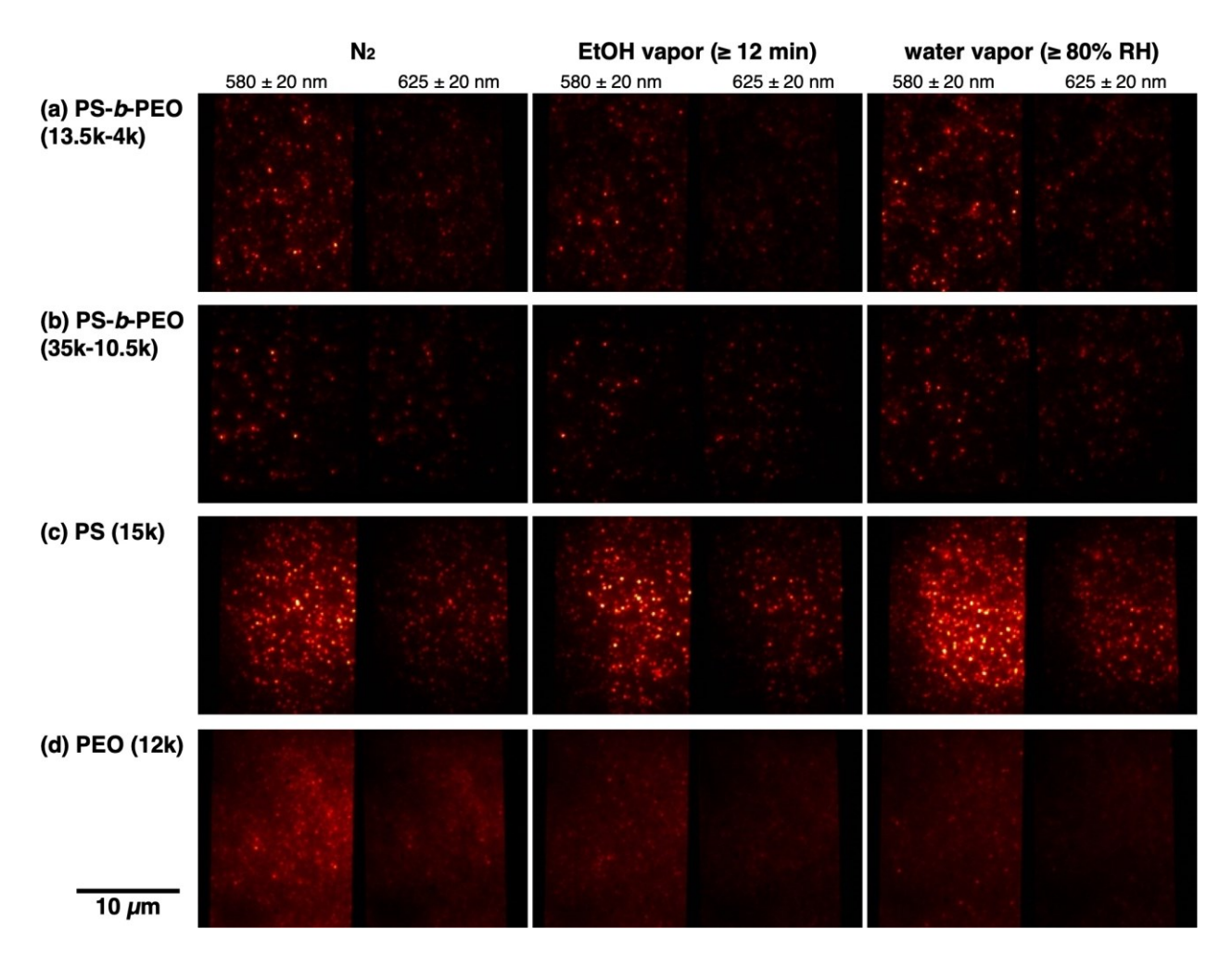


Figure 5. Typical single-molecule fluorescence images recorded in two spectral bands (left: 580 \pm 20 (nm); right: 625 \pm 20 (nm)) for thin PS-*b*-PEO (13.5k-4k), PS-*b*-PEO (35k-10.5k), PS, and PEO films (*ca.* 200 nm thick) containing 5 nM NR upon exposure to N₂, EtOH vapor (\geq 12 min), and water vapor (\geq 80% RH). Integration time: 1 s. The color scale (in counts) is 300 ~ 3,000 for all the images.

Single NR molecules in PS-b-PEO (35k-10.5k) films exhibited the reversible positive shift of E under EtOH vapor in contrast to those in PS films (**Figures 4c** and **S9bc**), consistent with the ensemble data (**Figure 4a**). This observation could be associated with EtOH-induced changes in the polarity/rigidity environment in the PS microdomains, possibly near the PS-PEO boundary region. In contrast, single-molecule E values at PS-b-PEO (13.5k-4k) negligibly changed under EtOH vapor owing to the significant contribution of impurity signals, as indicated by its E

distributions appearing very similar to those from NR-free films (**Figures S9a**). On the other hand, negligible changes in E for PS-b-PEO (35k-10.5k) and PS films under water vapor (**Figure 4d**) were consistent with the ensemble data (**Figure 4b**), and thus with the preferential distribution of NR molecules to PS microdomains in PS-b-PEO (35k-10.5k) films.

In conclusion, the two-color ensemble and single-molecule imaging verified that EtOH vapor can permeate through PEO microdomains, leading to changes in the polarity/rigidity of the environment around NR molecules that are possibly located at the PS-PEO interfacial region.

Diffusion of Hydrophilic Dyes at Polymer Thin Films under EtOH and Water Vapor. The results described above indicate that the solvent-induced thickness gain of PS-*b*-PEO films primarily reflected the swelling of the PEO microdomains. The swelling of the PEO microdomains was further assessed from the diffusion behavior of SRB, a fluorescence probe that preferentially partitions to the PEO microdomains, ⁵⁵ using SMT and FCS.

Figure 6 depicts the trajectories of single SRB molecules obtained from PS-b-PEO and PEO films under N_2 , EtOH vapor, and water vapor. Original SMT videos for the PS-b-PEO films are given as Videos S1-S10. SRB molecules in these films were immobile under N_2 (Figure 7), and were mobilized under EtOH vapor (Figure 6, EtOH (2 min)). Interestingly, prolonged exposure to EtOH vapor led to the reduction of their diffusion (Figure 6, EtOH (12 min)), as shown by a decrease in the percentage of mobile SRB molecules (Figure 7a) and also in D_{SMT} (Figures S10a and 7b). The initial enhancement and subsequent reduction of the solute diffusion were consistent with the initial swelling and subsequent deswelling of PS-b-PEO films as observed using spectroscopic ellipsometry (Figure 2ab). The deswelling may be driven by the crystallization of

PEO microdomains that would cause the gradual exclusion of ethanol from PEO chains owing to the low ethanol–PEO compatibility, as implied by the FTIR-ERS data (**Figure S5ab**).

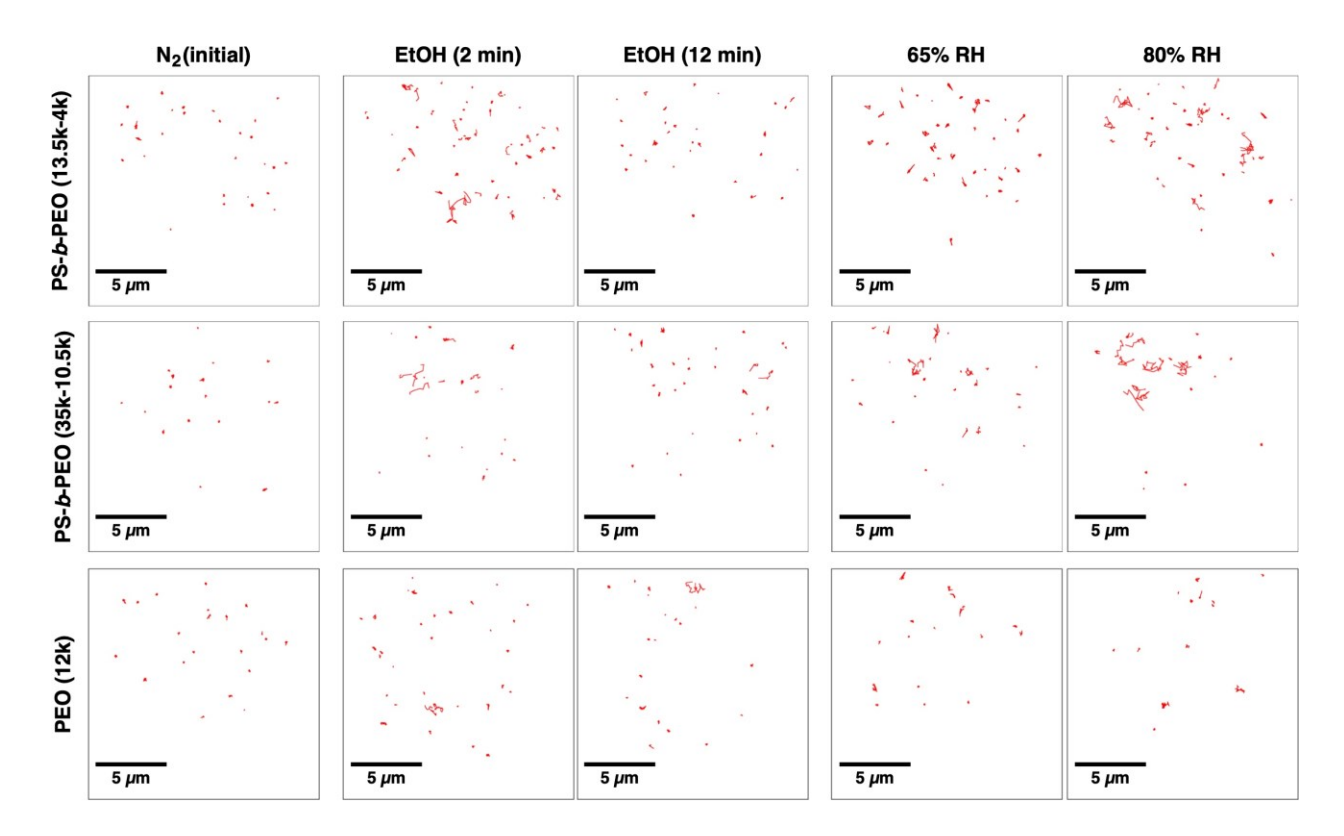


Figure 6. SMT trajectories obtained from thin films containing 1 nM SRB (230 nm thick for PS-b-PEO (13.5k-4k), 250 nm thick for PS-b-PEO (35k-10.5k), and 100 nm thick for PEO (12k)) under N₂, after exposure to EtOH vapor (2 min and 12 min) or water vapor (65% RH and 80% RH). The original SMT data for the PS-b-PEO films are given as **Videos S1-S10**.

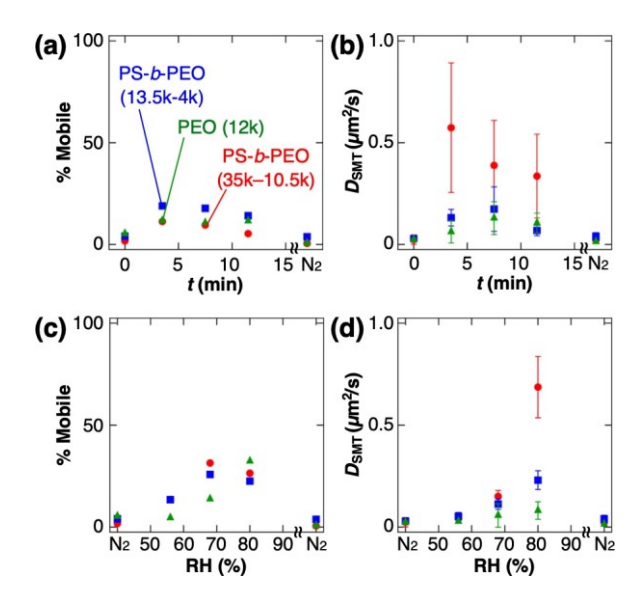


Figure 7. SMT results obtained from thin SRB-containing films (ca. 1 nM SRB) of PS-b-PEO (13.5k-4k) (ca. 230 nm thick), PS-b-PEO (35k-10.5k) (ca. 250 nm thick), and PEO (12k) (ca. 100 nm thick). The percentage and $D_{\rm SMT}$ of mobile molecules (a, b) at different EtOH vapor exposure times and (c, d) at different RH. The data on N₂ in the graphs were obtained under N₂ after solvent vapor exposure. The error bars in **Figure 7bd** represent 95% confidence intervals obtained from single molecule $D_{\rm SMT}$ values shown in **Figure S10**.

PEO films exhibited the enhancement of SRB diffusion under EtOH vapor, but did not clearly show the subsequent reduction of SRB diffusion in contrast to the PS-b-PEO films (**Figure 7ab**). The D_{SMT} values obtained from the PEO films were smaller than those from the PS-b-PEO films, possibly reflecting their higher crystallinity⁶⁸ than the PEO microdomains. Interestingly, PS-b-PEO (13.5k-4k) films afforded smaller D_{SMT} values than PS-b-PEO (35k-10.5k) under EtOH vapor (**Figure 7b**), which could reflect the larger contributions of PS-PEO interfacial region having lower solute diffusivity owing to the larger interface/volume ratio in the former. ^{22,25}

The diffusion of SRB molecules in PS-b-PEO and PEO films was enhanced by the longer duration of water vapor exposure, as shown by trajectory data acquired at 65% RH and 80% RH (**Figure 6**), which corresponded to exposure times of 3 min and 7 min in **Figure 2ab**. The percentage and D_{SMT} of mobile molecules gradually increased with increasing RH (**Figure 7cd**), consistent with the thickness increase of the PS-b-PEO films (**Figure 2abd**). These observations

resulted from the hydration of PEO that enhanced their chain mobility, as anticipated from the high PEO-water compatibility

It should be pointed out that SMT videos (Videos S2–S5, S7–S10) show many molecules that moved too quickly to yield trackable trajectories, which were likely to diffuse on the film surface. More quantitative assessment of the diffusion of SRB molecules in these films was explored using FCS. 56,63 FCS is based on the measurement of temporal fluctuations in the fluorescence intensity caused by the passage of diffusing molecules through the detection area, and thus is not affected by immobile impurities. In addition, the time resolution of the fluctuation measurements can be much higher than that of the single-molecule fluorescence video measurements, permitting the investigation of faster diffusion processes. Unfortunately, in contrast to SMT, FCS could not be used to monitor the minute-scale temporal processes, because relatively long measurement times (≥ 6 min) are required to obtain autocorrelation functions with sufficiently high S/N. In addition, FCS could not afford D values under EtOH vapor owing to the significant photobleaching of the dye molecules that were almost immobile after a relatively short vapor exposure, as discussed above (Figure 6).

Figure 8 shows typical FCS data obtained from (a) PS-*b*-PEO (13.5k-4k), (b) PS-*b*-PEO (35k-10.5k), and (c) PEO (12k) films after exposure to water vapor for > 10 min (\geq 80% RH). The autocorrelation functions obtained were fitted using the MEM^{63,71} to give 2-3 distinct diffusion components, as summarized in **Table 3**. In all cases, $D_{\text{FCS,fastest}}$ could be associated with SRB molecules diffusing in a thin water layer or swollen PEO chains on the film surface.⁶³ The $D_{\text{FCS,fastest}}$ values were significantly smaller than that of SRB molecules in aqueous solution (\approx 400 μ m²/s),⁷² implying the presence of interactions between the solute molecules and polymer chains/surfaces. The $D_{\text{FCS,medium}}$ values from the two PS-*b*-PEO films were in the range of *D* values

obtained using SMT, further confirming water-induced swelling of the PEO microdomains. The fractional contribution of $D_{FCS,medium}$ (f in **Table 3**) to the autocorrelation data was greater for PS-b-PEO (13.5k-4k) than for PS-b-PEO (35k-10.5k), consistent with the expected increase in importance of the PS-PEO interfaces in the shorter block copolymer. Note that the smaller D_{SMT} observed from PS-b-PEO (13.5k-4k) than PS-b-PEO (35k-10.5k) (**Table 3**) may be associated with the presence of $D_{FCS,slowest}$, which could bias the D_{SMT} values in the former. On the other hand, PEO films afforded two very fast diffusion components ($D_{FCS,faster}$ and $D_{FCS,medium}$), in addition to $D_{FCS,slowest}$ ($\sim D_{SMT}$) that could be assigned to dyes diffusing in the film (**Figure 8c** and **Table 3**). The observation of the two very fast components may be associated with the partial dissolution of the polymer by water.

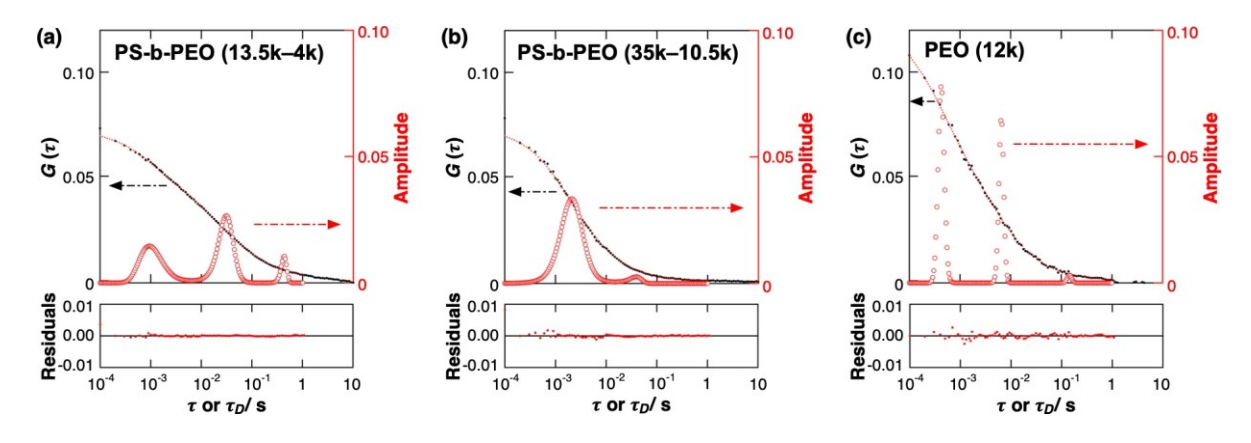


Figure 8. Typical FCS data (black dots) obtained on (a) PS-b-PEO (13.5k-4k), (b) PS-b-PEO (35k-10.5k), and (c) PEO (12k) films containing 50 nM SRB (300 nm thick) under a flow of water vapor (≥ 80% RH) at room temperature (*ca.* 20 °C). The fit and diffusion time distribution obtained using the maximum entropy method are given by a dashed red line and open red circles, respectively. The residuals of the fittings are also shown below. Note that **Figure 8a** was adapted with permission from Ref 63. Copyright 2022 Nature/Springer/Palgrave.

Table 3. Diffusion Coefficients (μm²/s) of SRB in Water-Vapor-Exposed Thin Polymer Films^{a)} Obtained Using SMT and FCS

	$D_{ m SMT}^{\ \ b)}$	$D_{ ext{FCS,fastest}}{}^{c)}$	$D_{ ext{FCS,medium}}{}^{c)}$	$D_{ ext{FCS,slowest}}{}^{c)}$
		$(f)^{e)}$	$(f)^{e)}$	$(f)^{e)}$
PS- <i>b</i> -PEO (13.5k–4k)	0.23 ± 0.08	28.4 ± 0.5 ^{d)}	0.85 ± 0.02^{d}	0.0571 ± 0.0004^{d}
		(0.42)	(0.51)	(0.07)
PS- <i>b</i> -PEO (35k–10.5k)	0.82 ± 0.20	12.4 ± 0.3 ^{d)}	0.76 ± 0.01 ^{d)}	NA
		(0.96)	(0.04)	
PEO (12k)	0.09 ± 0.05	57.5 ± 0.2^{d}	3.71 ± 0.01^{d}	$0.168 \pm 0.003^{d})$
, , ,		(0.60)	(0.38)	(0.02)

a) Upon exposure to water vapor for > 10 min, \geq 80% RH. b) 95% confidence interval from individual molecules (1 nM SRB) in thin films (230, 250, and 100 nm thick for PS-*b*-PEO (13.5k-4k), PS-*b*-PEO (35k-10.5k), and PEO (12k), respectively. c) Measured for 50 nM SRB in 300-nm thick films. d) 95% confidence interval obtained from the Gaussian fit of the D_{FCS} distribution. e) Fraction of the D_{FCS} component.

Conclusions

In this study, we revealed the unique swelling properties of block copolymer microdomains in thin PS-b-PEO films through systematic spectroscopic and microscopic measurements under N₂, EtOH and water vapors. We observed a 6–9% increase in the thickness of PS-b-PEO films under EtOH vapor using *in situ* spectroscopic ellipsometry, which was unexpected considering the poor compatibility of ethanol with PS and PEO. The maximum thickness gain was close to that observed upon exposure to water vapor, suggesting that the thickness increase was controlled by the swelling of PEO microdomains (20–30 nm in domain spacing) in PS-b-PEO films. Interestingly, PS-b-PEO films exposed to EtOH vapor exhibited a gradual thickness reduction after an initial quick thickness increase, which was not observed for those exposed to water vapor. We employed a series of fluorescence techniques to gain detailed insights into the swelling behaviors of the PS-b-PEO films. Two-color fluorescence imaging with NR verified the penetration of ethanol vapor through PEO microdomains, and revealed the larger EtOH-induced polarity/rigidity changes for the smaller PS-b-PEO owing to the larger interface/volume ratio associated with its

smaller microdomains. SMT revealed the initial enhancement and subsequent reduction of SRB diffusion in PS-b-PEO films upon exposure to EtOH vapor, which were consistent with the initial swelling and subsequent deswelling of the films observed using spectroscopic ellipsometry. The larger PS-b-PEO exhibited more significant enhancement of SRB diffusion upon exposure to EtOH vapor, which could reflect the smaller interface/volume ratio with the lower solute diffusivity at the PS-PEO interfacial region. On the other hand, the diffusion of SRB in PS-b-PEO films under water vapor was enhanced at higher RH owing to the swelling of the PEO microdomains, as expected from the high compatibility of water with PEO. FCS-MEM could be used to measure quickly diffusing SRB molecules on/in the films under water vapor, in contrast to SMT. The ethanol-induced swelling of the PEO microdomains was attributable to their amorphous nature, as suggested by the FTIR-ERS data, possibly owing to suppressed microphase separation at the PS-PEO interfacial region 16,17,23 and the reduced entanglement of polymer chains in the spin-cast films.⁶⁴ The crystallization of PEO microdomains observed after water vapor exposure and subsequent evaporation (Figure S5ab) may play a role in the improved vertical orientation of PEO microdomains in PS-b-PEO films upon solvent vapor annealing.

In addition, spectroscopic ellipsometry and fluorescence microscopy results provided valuable information on the structural nature of the PS-*b*-PEO films. The observation of the 6–9% thickness gain independent of film thicknesses indicated that the PEO microdomains in the PS-*b*-PEO films penetrated from the air–film to film–substrate interfaces. The relatively small thickness gain (6–9%) of the PS-*b*-PEO films was attributed to the suppression of the PEO swelling by the unswellable PS microdomains.¹⁹ This study shows the applicability of a series of fluorescence methods for comprehensive understanding of the unique physicochemical properties of block copolymer microdomains. The detailed knowledge of the swelling properties of block

copolymer microdomains will help achieve the optimal performance of these materials for their

applications as polyelectrolytes and chemical separation membranes.

Associated Content

Supporting Information

The Supporting Information is available free of charge on the ACS Publication website at DOI:.

Experimental details on wide-field fluorescence and FCS measurements, experimental setups for

spectroscopic ellipsometry (Figure S1) and fluorescence microscopy (Figure S2), AFM images

of PS-b-PEO films (Figure S3), reflective SAXS data of PS-b-PEO films (Figure S4), FTIR

spectra of PS-b-PEO and PEO films (Figure S5), ensemble fluorescence images of NR-doped

films (Figure S6), single-molecule fluorescence images of NR-free films (Figure S7), histograms

of fluorescence intensity and E values from single fluorescent spots in NR-doped and NR-free

films (**Figures S8** and **S9**, respectively), histograms of D_{SMT} values of single mobile molecules in

SRB-doped films (Figure S10), and SMT videos (Videos S1-S10).

Author Information

Corresponding Authors

* E-mail: higgins@ksu.edu. Phone: 785-532-6371 (D.A.H.)

* E-mail: ito@ksu.edu. Phone: 785-532-1451. Fax: 785-532-6666 (T.I.).

ORCID

28

Daniel A. Higgins: 0000-0002-8011-2648

Takashi Ito: 0000-0001-7443-3157

Notes

The authors declare no competing financial interest.

Acknowledgement

The authors gratefully acknowledge Office of Basic Energy Sciences of the U.S. Department

of Energy (DE-SC0002362) for financial support to this work. They thank Mr. James Hilfiker (J.

A. Woollam), Dr. Javier Seravalli (Redox Biology Center and Department of Biochemistry,

University of Nebraska, Lincoln) and Dr. Shah Valloppilly (Nebraska Nanoscale Facility: National

Nanotechnology Coordinated Infrastructure, University of Nebraska, Lincoln) for their help with

the spectroscopic ellipsometry, ICP-MS and SAXS experiments, respectively. They also thank

Dr. Todd Emrick (University of Massachusetts, Amherst) for his suggestion of the possible

presence of impurities in the polymers. The FTIR spectrometer employed was purchased through

a financial support from the National Science Foundation (CHE-1709285). The SAXS

measurements were performed in the Nebraska Nanoscale Facility: National Nanotechnology

Coordinated Infrastructure and the Nebraska Center for Materials and Nanoscience (and/or

NERCF), which are supported by the National Science Foundation under Award ECCS: 2025298,

and the Nebraska Research Initiative.

29

References

- Bates, F. S.; Fredrickson, G. H. Block Copolymers Designer Soft Materials. *Phys. Today* **1999**, *52*, 32–38.
- Bates, C. M.; Bates, F. S. 50th Anniversary Perspective: Block Polymers Pure Potential. *Macromolecules* **2017**, *50*, 3-22.
- Ruzette, A. V.; Leibler, L. Block Copolymers in Tomorrow's Plastics. *Nat. Mater.* **2005**, *4*, 19-31.
- 4 Creton, C.; Hu, G.; Deplace, F.; Morgret, L.; Shull, K. R. Large-Strain Mechanical Behavior of Model Block Copolymer Adhesives. *Macromolecules* **2009**, *42*, 7605–7615.
- Bang, J.; Jeong, U.; Ryu, D. Y.; Russell, T. P.; Hawker, C. J. Block Copolymer Nanolithography: Translation of Molecular Level Control to Nanoscale Patterns. *Adv. Mater.* **2009**, *21*, 4769–4792.
- 6 Cummins, C.; Ghoshal, T.; Holmes, J. D.; Morris, M. A. Strategies for Inorganic Incorporation Using Neat Block Copolymer Thin Films for Etch Mask Function and Nanotechnological Application. *Adv. Mater.* **2016**, *28*, 5586–5618.
- Li, C.; Li, Q.; Kaneti, Y. V.; Hou, D.; Yamauchi, Y.; Mai, Y. Self-Assembly of Block Copolymers towards Mesoporous Materials for Energy Storage and Conversion Systems. *Chem. Soc. Rev.* **2020**, *49*, 4681–4736.
- 8 Loo, W. S.; Balsara, N. P. Organizing Thermodynamic Data Obtained from Multicomponent Polymer Electrolytes: Salt-Containing Polymer Blends and Block Copolymers. J. Polym. Sci., Part B: Polym. Phys. 2019, 57, 1177–1187.
- 9 Young, W. S.; Kuan, W. F.; Epps, T. H., III. Block Copolymer Electrolytes for Rechargeable Lithium Batteries. *J. Polym. Sci. B: Polym. Phys.* **2014**, *52*, 1–16.
- Zhang, Y.; Sargent, J. L.; Boudouris, B. W.; Phillip, W. A. Nanoporous Membranes Generated from Self-Assembled Block Polymer Precursors: Quo Vadis? *J. Appl. Polym. Sci.* **2015**, *132*, 41683.
- Nunes, S. P. Block Copolymer Membranes for Aqueous Solution Applications. *Macromolecules* **2016**, *49*, 2905–2916.
- Zhou, J.; Wang, Y. Selective Swelling of Block Copolymers: An Upscalable Greener Process to Ultrafiltration Membranes? *Macromolecules* **2020**, *53*, 5–17.
- Hampu, N.; Werber, J. R.; Chan, W. Y.; Feinberg, E. C.; Hillmyer, M. A. Next-Generation Ultrafiltration Membranes Enabled by Block Polymers. *ACS Nano* **2020**, *14*, 16446–16471.
- Ito, T. Block Copolymer-Derived Monolithic Polymer Films and Membranes Comprising Self-Organized Cylindrical Nanopores for Chemical Sensing and Separations. *Chem.*–*Asian J.* **2014**, *9*, 2708–2718.
- Ito, T.; Ghimire, G. Electrochemical Applications of Microphase-Separated Block Copolymer Thin Films. *ChemElectroChem* **2018**, *5*, 2937–2953.
- Huang, P.; Guo, Y.; Quirk, R. P.; Ruan, J.; Lotz, B.; Thomas, E. L.; Hsiao, B. S.; Avila-Orla, C. A.; Sics, I.; Cheng, S. Z. D. Comparison of Poly(ethylene oxide) Crystal Orientation and Crystallization Behaviors in Nano-confined Cylinders Constructed by a Poly(ethylene oxide)-b-Polystyrene Diblock Copolymer and a Blend of Poly(ethylene oxide)-b-Polystyrene and Polystyrene. *Polymer* **2006**, *47*, 5457–5466.
- Beaudoin, E.; Phan, T. N. T.; Robinet, M.; Denoyel, R.; Davidson, P.; Bertin, D.; Bouchet, R. Effect of Interfaces on the Melting of PEO Confined in Triblock PS-*b*-PEO-*b*-PS Copolymers. *Langmuir* **2013**, *29*, 10874–10880.

- 18 Chen, H.-L.; Hsiao, S.-C.; Lin, T.-L.; Yamauchi, K.; Hasegawa, H.; Hashimoto, T. Microdomain-Tailored Crystallization Kinetics of Block Copolymers. *Macromolecules* **2001**, *34*, 671–674.
- Oparaji, O.; Minelli, M.; Zhu, C.; Schaible, E.; Hexemer, A.; Hallinan, D. T., Jr. Effect of Block Copolymer Morphology on Crystallization and Water Transport. *Polymer* **2017**, *120*, 209–216.
- Alcoutlabi, M.; McKenna, G. B. Effects of Confinement on Material Behavior at the Nanometre Size Scale. *J. Phys.: Condens. Matter* **2005**, *17*, R461–R524.
- Lotz, B.; Miyoshi, T.; Cheng, S. Z. D. 50th Anniversary Perspective: Polymer Crystals and Crystallization: Personal Journeys in a Challenging Research Field. *Macromolecules* **2017**, 50, 5995–6025.
- Pandey, A.; Mullin, S.; Gomez, E. D.; Wanakule, N.; Chen, V. L.; Hexemer, A.; Pople, J.; Balsara, N. P. Effect of Molecular Weight and Salt Concentration on Conductivity of Block Copolymer Electrolyte. *Macromolecules* **2009**, *42*, 4632–4637.
- Yuan, R.; Teran, A. A.; Gurevitch, I.; Mullin, S. A.; Wanakule, N. S.; Balsara, N. P. Ionic Conductivity of Low Molecular Weight Block Copolymer Electrolytes. *Macromolecules* **2013**, *46*, 914–921.
- Gomez, E. D.; Panday, A.; Feng, E. H.; Chen, V.; Stone, G. M.; Minor, A. M.; Kisielowski, C.; Downing, K. H.; Borodin, O.; Smith, G. D.; et al. Effect of Ion Distribution on Conductivity of Block Coplolymer Electrolytes. *Nano Lett.* **2009**, *9*, 1212–1216.
- Ganesan, V.; Pyramitsyn, V.; Bertoni, C.; Shah, M. Mechanisms Underlying Ion Transport in Lamellar Block Copolymer Membranes. *ACS Macro. Lett.* **2012**, *1*, 513–518.
- Dobies, M.; Makrocka-Rydzyk, M.; Jenczyk, J.; Jarek, M.; Spontak, R. J.; Jurga, S. Molecular Dynamics Study of Polystyrene-*b*-Poly(ethylene oxide) Asymmetric Diblock Copolymer Systems. *Langmuir* **2017**, *33*, 8856–8868.
- 27 Richter, D.; Kruteva, M. Polymer Dynamics under Confinement. *Soft Matter* **2019**, *15*, 7316–7349.
- Alegria, A.; Colmenero, J. Dielectric Relaxation of Polymers: Segmental Dynamics under Structural Constraints. *Soft Matter* **2016**, *12*, 7709–7725.
- Hiemenz, P. C.; Lodge, T. P. *Polymer Chemistry, 2nd Ed.*; CRC Press, 2007.
- 30 Sinturel, C.; Vayer, M.; Morris, M.; Hillmyer, M. A. Solvent Vapor Annealing of Block Polymer Thin Films. *Macromolecules* **2013**, *46*, 5399–5415.
- Posselt, D. *et al.* Restructuring in Block Copolymer Thin Films: In Situ GISAXS Investigations during Solvent Vapor Annealing. *Prog. Polym. Sci.* **66**, 80–115 (2017).
- 32 Huang, C., Zhu, Y. & Man, X. Block Copolymer Thin Films. *Phys. Rep.* **932**, 1–36 (2021).
- Pula, P., Leniart, A. & Majewski, P. W. Solvent-Assisted Self-Assembly of Block Copolymer Thin Films. *Soft Matter* **18**, 4042–4066 (2022).
- Ogieglo, W.; Wormeester, H.; Eichhorn, K.-J.; Wessling, M.; Benes, N. E. In Situ Ellipsometry Studies on Swelling of Thin Polymer Films: A Review. *Prog. Polym. Sci.* **2015**, *42*, 42–78.
- Ogieglo, W.; Stenbock-Fermor, A.; Juraschek, T. M.; Bogdanova, Y.; Benes, N.; Tsarkova, L. A. Synergic Swelling of Interactive Network Support and Block Copolymer Films during Solvent Vapor Annealing. *Langmuir* **2018**, *34*, 9950–9960.
- Jin, C.; Olsen, B. C.; Luber, E. J.; Buriak, J. M. Nanopatterning via Solvent Vapor Annealing of Block Copolymer Thin Films. *Chem. Mater.* **2017**, *29*, 176–188.

- Hoang, D. T.; Yang, J.; Paeng, K.; Kwon, Y.; Kweon, O. S.; Kaufman, L. J. In Situ Multi-Modal Monitoring of Solvent Vapor Swelling in Polymer Thin Films. *Rev. Sci. Instrum.* **2016**, *87*, 015106.
- Kim, S. H.; Misner, M. J.; Xu, T.; Kimura, M.; Russell, T. P. Highly Oriented and Ordered Arrays from Block Copolymers via Solvent Evaporation. *Adv. Mater.* **2004**, *16*, 226–231.
- Bang, J.; Kim, B.; Stein, G.; Russell, T.; Li, X.; Wang, J.; Kramer, E.; Hawker, C. Effect of Humidity on the Ordering of PEO-Based Copolymer Thin Films. *Macromolecules* **2007**, 40, 7019-7025.
- 40 Kim, B.; Hong, S. W.; Park, S.; Xu, J.; Hong, S. K.; Russell, T. P. Phase Transition Behavior in Thin Films of Block Copolymers by Use of Immiscible Solvent Vapors. *Soft Matter* **2011**, *7*, 443–447.
- Mokarian-Tabari, P.; Collins, T. W.; Holmes, J. D.; Morris, M. A. Cyclical "Flipping" of Morphology in Block Copolymer Thin Films. *ACS Nano* **2011**, *5*, 4617–4623.
- Raybin, J. G.; Sibener, S. J. In Situ Visualization of Solvent Swelling Dynamics in Block Copolymer Films with Atomic Force Microscopy. *Macromolecules* **2019**, *52*, 5985–5994.
- Sapkota, D. R.; Tran-Ba, K.-H.; Elwell-Cuddy, T.; Higgins, D. A.; Ito, T. Single-Molecule Tracking Study of the Permeability and Transverse Width of Individual Cylindrical Microdomains in Solvent-Swollen Polystyrene-*block*-poly(ethylene oxide) Films. *J. Phys. Chem. B* **2016**, *120*, 12177–12183.
- Coceancigh, H.; Higgins, D. A.; Ito, T. Optical Microscopic Techniques for Synthetic Polymer Characterization. *Anal. Chem.* **2019**, *91*, 405–424.
- Park, W. I.; Kim, J. M.; Jeong, J. W.; Jung, Y. S. Deep-Nanoscale Pattern Engineering by Immersion-Induced Self-Assembly. *ACS Nano* **2014**, *8*, 10009–10018.
- 46 Modi, A.; Bhaway, S. M.; Vogt, B. D.; Douglas, J. F.; Al-Enizi, A.; Elzatahry, A.; Sharma, A.; Karim, A. Direct Immersion Annealing of Thin Block Copolymer Films. ACS Appl. Mater. Interfaces 2015, 7, 21639–21645.
- Errede, L. A. Polymer Swelling. 7. A Molecular Interpretation of Polymer Swelling. *J. Phys. Chem.* **1989**, *93*, 2668–2671.
- Graham, N. B.; Nwachuku, N. E.; Walsh, D. J. Interaction of Poly(ethylene oxide) with Solvents: 1. Preparation and Swelling of a Crosslinked Poly(ethylene oxide) Hydrogel. *Polymer* **1982**, *23*, 1345–1349.
- Yang, H.; Guo, L.; Wang, Z.; Yan, N.; Wang, Y. Nanoporous Films with Superior Resistance to Protein Adsorption by Selective Swelling of Polystyrene-block-Poly(ethylene oxide). *Ind. Eng. Chem. Res.* **2016**, *55*, 8133–8140.
- Yang, H.; Wang, Z.; Lan, Q.; Wang, Y. Antifouling Ultrafiltration Membranes by Selective Swelling of Polystyrene/Poly(ethylene oxide) Block Copolymers. *J. Membr. Sci.* **2017**, *542*, 226–232.
- Hou, Y.; Bardo, A. M.; Martinez, C.; Higgins, D. A. Characterization of Molecular Scale Environments in Polymer Films by Single Molecule Spectroscopy. *J. Phys. Chem. B* **2000**, *104*, 212–219.
- Hou, Y.; Higgins, D. A. Single Molecule Studies of Dynamics in Polymer Thin Films and at Surfaces: Effect of Ambient Relative Humidity. *J. Phys. Chem. B* **2002**, *106*, 10306–10315.
- Kumarasinghe, R.; Higgins, E. D.; Ito, T.; Higgins, D. A. Spectroscopic and Polarization-Dependent Single-Molecule Tracking Reveal the One-Dimensional Diffusion Pathways in Surfactant-Templated Mesoporous Silica. *J. Phys. Chem. C* **2016**, *120*, 715–723.

- Xu, H.; Nagasaka, S.; Kameta, N.; Masuda, M.; Ito, T.; Higgins, D. A. Spectroscopic Imaging Studies of Nanoscale Polarity and Mass Transport Phenomena in Self-Assembled Organic Nanotubes. *Phys. Chem. Chem. Phys.* **2017**, *19*, 20040–20048.
- Tran-Ba, K.-H.; Finley, J. J.; Higgins, D. A.; Ito, T. Single-Molecule Tracking Studies of Millimeter-Scale Cylindrical Domain Alignment in Polystyrene–Poly(ethylene oxide) Diblock Copolymer Films Induced by Solvent Vapor Penetration. *J. Phys. Chem. Lett.* **2012**, *3*, 1968–1973.
- Higgins, D. A.; Park, S. C.; Tran-Ba, K.-H.; Ito, T. Single-Molecule Investigations of Morphology and Mass Transport Dynamics in Nanostructured Materials. *Annu. Rev. Anal. Chem.* 2015, 8, 193–216.
- Farzin, S.; Sarella, A.; Yandrasits, M. A.; Dishari, S. K. Fluorocarbon-Based Ionomers with Single Acid and Multiacid Side Chains at Nanothin Interfaces. *J. Phys. Chem. C* **2019**, *123*, 30871–30884.
- Ito, T.; Coceancigh, H.; Yi, Y.; Sharma, J. N.; Parks, F. C.; Flood, A. H. Nanoporous Thin Films Formed from Photocleavable Diblock Copolymers on Gold Substrates Modified with Thiolate Self-Assembled Monolayers. *Langmuir* **2020**, *36*, 9259–9268.
- Tran-Ba, K.-H.; Higgins, D. A.; Ito, T. Single-Molecule Tracking Studies of Flow-Induced Microdomain Alignment in Cylinder-Forming Polystyrene–Poly(ethylene oxide) Diblock Copolymer Films. *J. Phys. Chem. B* **2014**, *118*, 11406–11415.
- Tran-Ba, K.-H.; Higgins, D. A.; Ito, T. Fluorescence Recovery after Photobleaching and Single-Molecule Tracking Measurements of Anisotropic Diffusion within Identical Regions of a Cylinder-Forming Diblock Copolymer Film. *Anal. Chem.* **2015**, *87*, 5802–5809.
- Kim, H.-H.; Song, N. W.; Park, T. S.; Yoon, M. Laser Scanning Confocal Microscope (LSCM)-Fluorescence Spectral Properties of Nile Red Embedded in Polystyrene Film of Different Thickness. *Chem. Phys. Lett.* **2006**, *432*, 200–204.
- 62 Giri, D.; Hanks, C. N.; Collinson, M. M.; Higgins, D. A. Single-Molecule Spectroscopic Imaging Studies of Polarity Gradients Prepared by Infusion-Withdrawal Dip-Coating. *J. Phys. Chem. C* **2014**, *118*, 6423–6432.
- Xue, L.; Jin, S.; Nagasaka, S.; Higgins, D. A.; Ito, T. Investigation of Molecular Diffusion at Block Copolymer Thin Films Using Maximum Entropy Method-Based Fluorescence Correlation Spectroscopy and Single Molecule Tracking. *J. Fluoresc.* **2022**, 32, 1779–1787.
- Barbero, D. R.; Steiner, U. Nonequilibrium Polymer Rheology in Spin-Cast Films. *Phys. Rev. Lett.* **2009**, *102*, 248303.
- Miyazawa, T.; Ideguchi, Y.; Fukushima, K. Molecular Vibrations and Structure of High Polymers. 3. Polarized Infrared Spectra, Normal Vibrations, and Helical Conformation of Polyethylene Glycol. *J. Chem. Phys.* **1962**, *37*, 2764–2776.
- Dissanayake, M. A. K. L.; Frech, R. Infrared Spectroscopic Study of the Phases and Phase Transitions in Poly(ethylene oxide) and Poly(ethylene oxide)—Lithium Trifluoromethanesulfonate Complexes. *Macromolecules* **1995**, *28*, 5312–5319.
- Perera, D. M. N. T.; Pandey, B.; Ito, T. Electrochemical Impedance Spectroscopy Studies of Organic-Solvent-Induced Permeability Changes in Nanoporous Films Derived from a Cylinder-Forming Diblock Copolymer. *Langmuir* **2011**, *27*, 11111–11117.
- 68 Tran-Ba, K.-H.; Willis, R. E.; Foreman, K.; Ajmani, K.; Gujarati, P. Single-Molecule Tracking in Poly(Ethylene Oxide) Films: Revealing the Effects of Molecular Weight,

- Network Plasticization, and Thermal Annealing on Anionic Dye Diffusion. *J. Phys. Chem. B* **2021**, *125*, 382–392.
- Deye, J. F.; Berger, T. A.; Anderson, A. G. Nile Red as a Solvatochromic Dye for Measuring Solvent Strength in Normal Liquids and Mixtures of Normal Liquids with Supercritical and Near Critical Fluids. *Anal. Chem.* **1990**, *62*, 615–622.
- Dutta, A. K.; Kamada, K.; Ohta, K. Spectroscopic Studies of Nile Red in Organic Solvents and Polymers. *J. Photochem. Photobiol. A* **1996**, *93*, 57–64.
- Sengupta, P.; Garai, K.; Balaji, J.; Periasamy, N.; Maiti, S. Measuring Size Distribution in Highly Heterogeneous Systems with Fluorescence Correlation Spectroscopy. *Biophys. J.* **2003**, *84*, 1977–1984.
- Gendron, P. O.; Avaltroni, F.; Wilkinson, K. J. Diffusion Coefficients of Several Rhodamine Derivatives as Determined by Pulsed Field Gradient-Nuclear Magnetic Resonance and Fluorescence Correlation Spectroscopy. *J. Fluoresc.* **2008**, *18*, 1093–1101.

TOC Graphic

